Small-signal Modelling and Tuning of Synchronverter-based wind energy conversion systems

Henrik Høstmark, Mohammad Amin (corresponding author)
Department of Electric Power Engineering, NTNU
7491 Trondheim, Norway, email: mohammad.amin@ntnu.no

Abstract: The Synchronverter technique is an example of a virtual synchronous machine-based control method for PWM controlled power electronic converters that enable converters to mimic the behavior of a synchronous generator (SG). It is based on the well-established mathematical model of an SG and should equip converter connected generation with the capabilities of providing the grid with ancillary services such as frequency/voltage support due to the inherent capabilities of the SG. In this paper, the Synchronverter control method is applied to a wind energy conversion system (WECS) connected to the grid using back-to-back converters. The mathematical models of the control system for both the rectifier side and the inverter side are elaborated and used to derive the required transfer functions. A tuning procedure is proposed, using the transfer functions of the system, to enable a fast and easy adaption of the control method to power systems with different parameters. Simulations have been performed to validate both the functioning of the proposed tuning procedure and the ability of the WECS to provide the grid with ancillary services. The results are promising, showing the controllers yielding fast and accurate responses to contingencies and changes in power set-points without steady-state deviations.

Keywords: Wind Energy, Synchronverter, Frequency response, Back-to-back converters
Data availability statement: The data that support the findings of this study are available from the corresponding author upon reasonable request.

1 Introduction

In recent years the power system has started the transition from a centralized structure dominated by conventional generation, to a distributed structure, dominated by converter connected, renewable generation. In this transition, one of the most promising and fastest-growing energy sources is wind power, which is often connected to the grid using power electronic converters due to its intermittent- and uncontrollable nature. The increased interest in wind power can be accredited to political, economical and technical reasons as new climate policies favors renewable energy, the Levelized cost of electricity for wind power in Germany, Britain and France drops below coal-fired electricity and more efficient turbines are being developed, all leading to wind power to become the leading energy technology in Europe measured by installed capacity in 2019 [1–3].

Modern wind turbines are divided into two categories based on the operating type; fixed speed wind turbines and variable speed wind turbines. Variable speed turbines are preferred due to more control flexibility and improved system efficiency and power quality [4, 5]. The most used topologies for variable speed wind turbines are doubly-fed induction generators and fully-rated converter wind turbines with permanent magnet synchronous generators, and both of these topologies often use PWM controlled back-to-back converters for connection to the grid [6].

The new system topology, dominated by converter connected generation, creates new challenges related to system stability in the form of less inertia and easily adjustable energy sources. This requires new types of grid control and grid regulation, resulting in more and more countries establishing new grid codes and requirements for what types of support functions a unit connected through power electronics must be able to supply. This is especially important for maintaining the security and stability of the power grid also in a future with less conventional generation and higher penetration of renewables.

A proposed solution to these challenges is to control converters, both rectifiers and inverters, to mimic synchronous machines. One such virtual synchronous machine (VSM) is the Synchronverter first proposed by Zhong and Weiss [7, 8]. The use of VSMs seems like a promising method of enabling converter connected generation to provide the grid with ancillary services, such as inertial response and frequency control, formerly only provided by conventional synchronous machines. While the concept of controlling back-to-back converters as Synchronverters when connecting wind power to the grid was first proposed by Ma and Zhong [9], the concept was only

proven for a relatively small system. Chandra Bose and P.B further applies the synchronverter technique to a HVDC system in [10], but no detailed discussion on controller parameters is provided.

The proposed solution should therefore be applied to a larger system with more realistic parameters. To enable this, an easy and precise method of adapting controller parameters to any given system should be proposed. Besides, the proposed solution by Ma et al [6, 9] uses sinusoidal tracking algorithms (STAs) to enable synchronization with the grid. Such STAs have several disadvantages such as requiring increased controller complexity adding unnecessary computational burden to the controller, being more prone to numerical deviations in the digital controller and including even more parameters that needs to be chosen for the highly non-linear algorithm to ensure the convergence speed and accuracy of the algorithm. Several methods of choosing parameters for Synchronverter controlled converters exist in the literature.

In the original Synchronverter, Zhong and Weiss [8] chooses parameters using empirical formulas and pre-chosen time constants, meaning trial and error must be applied when choosing the parameters used in the formulas. To counter this, Wu et al [11] proposes a general tuning algorithm for virtual synchronous machines that can be modified and adapted to the syncrhonverter. Dong and Chen [12] proposes an enhanced self-synchronization technique using a virtual resistance branch and a damping correction loop with parameters chosen based entirely on the trial and error method, while Rosso et al [13] and Dong and Chen [14] find parameters based on the linearized system state-space model.

Dong et al investigates a self-synchronizing Synchronverter in [15] where practical guidance on favorable controller settings to achieve fast self synchronization and well-tuned parameters are provided. However, also here only the inverter side is considered in the investigation. Brahma et al [16] explains the impact of system parameters such as the moment of inertia, integrator gain, droop coefficients and reference power. Here, the coupling effect between the frequency loop and the voltage loop of the control structure is identified, and it is also stated that optimum values of the parameters need to be found to ensure safe and efficient operation of the system. No work is however done to eliminate the coupling effect or find such optimal control values.

Dong and Chen [17] also proposes a method to directly compute controller parameter values in a Synchronverter augmented with a damping correction. Here, avoidance of trial-and-error procedures and achievement of precise pole placement is obtained, but the work focus only on the Active Power Loop (APL) of inverter control. Also, Zhang et al [18] proposes a parameter design method that includes the effects of low-pass filters. However, the authors focus only on single-phase synchronverter controlled inverters. Vasudevan and Ramachandaramurthy uses a linearized state-space model in [19] to find optimal values of the controller parameters such as the inertia constant, but no solution for tuning the parameters of the PI controller is provided. Further, Mehrasa et al discuss an implementation of a single synchronous controller for power electronics integrating renewables in [20, 21]. These references do however only consider inverter control, making the method unfeasbile for back-to-back converters in its current form. In addition the proposed control structure include multiple PI controllers, yielding even more parameters needing tuning.

Lastly, Wei et al [22] obtains a small-signal model of a Synchronverter controlled inverter and then uses the "optimal second-order system" method, choosing the dampening ratio of the system, and then use the Eigen equation to find eigenvalues yielding the desired response. However, again the authors do not look at rectifier controls. Therefore, based on the literature and to the best of the authors' knowledge, no work has been done on finding the transfer functions and developing a method of choosing controller parameters for Synchronverter controlled rectifiers, and adapting this to back-to-back converters integrating a large scale wind turbine.

In this paper, a tuning method of Synchronverter controller parameters for back-to-back converters is proposed. More specifically the contribution devolves around tuning the control system for the rectifier side of the back-to-back converters. Using the transfer functions of the control systems a procedure is developed to enable a fast and easy adaption of the Synchronverter to wind power systems with different parameters. Based on the small-signal model of a synchronverter controlled inverter, the small-signal model of a Synchronverter controlled rectifier is established, and a method of tuning the PI controller is proposed to ensure fast a precise control of the DC link voltage. The basis for the proposed method is a large scale wind energy conversion system connected to the grid through back-to-back converters. Here, the rotor side rectifier controls the DC link voltage and the grid side inverter controls the injected active- and reactive power to the grid based on the maximum power point of the wind turbine and reactive power consumption at the grid. The transfer functions are obtained using a small signal model based on the mathematical model of the control system and the block diagrams. To validate the functioning of the tuning procedure, a fictitious system is implemented in the MATLAB/Simulink environment and tested for different voltage and frequency events to ensure that the controls behave as designed.

The rest of the paper is structured as follows: The basics of a Synchronverter based wind energy conversion system and the Synchronverter control technology are outlined in Section 2. The transfer functions and the tuning procedure are explained in Section 3, before simulation results are provided in Section 5. Finally, this

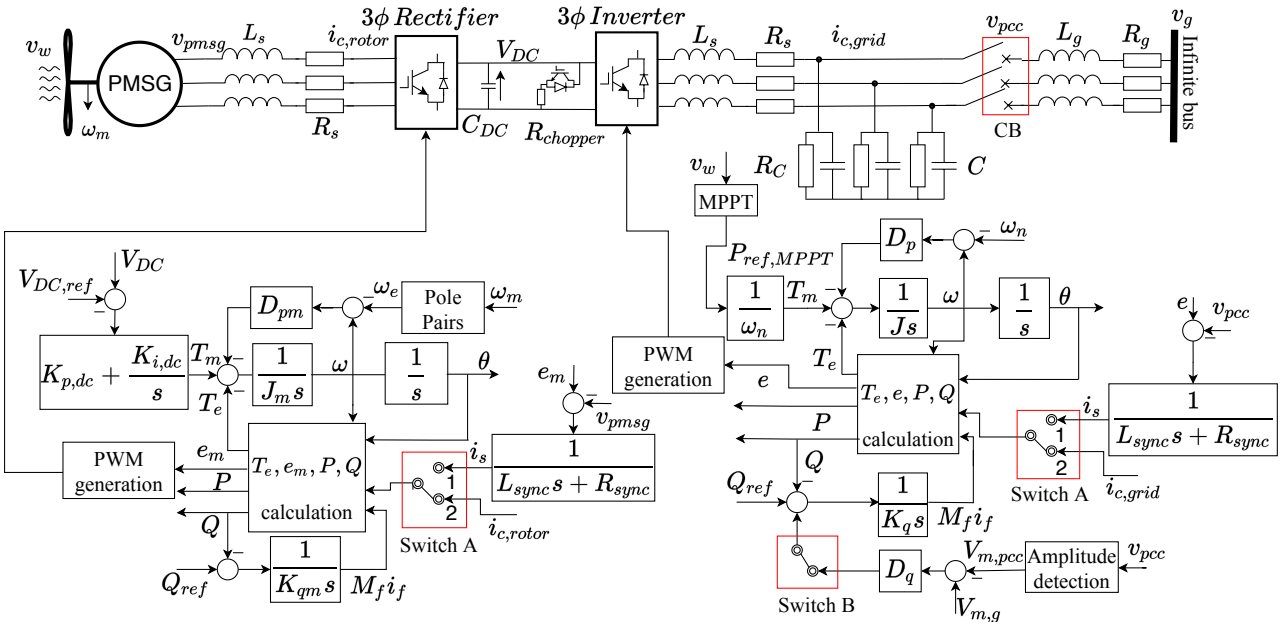

Figure 1: System topology of a wind turbine connected to the grid through back-to-back converters, including control systems modified from [9, 23, 24].

work is concluded in Section 6.

2 Synchronverter-based WECS

In this paper, a full-scale type-four WECS is investigated, which is connected to the ac grid through a two-level voltage source converter (VSC). The system is shown in Fig. 1. Synchronverter control technology has been adopted for both the grid side converter and the rotor side converter. The control architectures of the converters are as follows. 1) The grid side converter is used to regulate the active power and reactive power injection to the grid. The maximum power tracking algorithm has been implemented to the grid side converter. 2) The rotor side converter is used to control the voltage of the WECS dc-bus.

2.1 Control of the grid side converter

The implementation of grid side converter controller is based on the synchronverter proposed by Zhong and Weiss [8]. An idealized three-phase round rotor SG is recalled for the purpose of implementing the synchronverter control strategy [25]. The stator winding is assumed to be a concentrated coil having self-inductance L and mutual-inductance M with a typical value of $1/2L$. The field winding is assumed to be a concentrated coil having self-inductance L_f. The phase terminal voltage, $v_{abc} = [v_a \quad v_b \quad v_c]^T$ can be written as

$$v_{abc} = -R_s i_{abc} - L_s \frac{di_{abc}}{dt} + e_{abc} \tag{1}$$

where, $i_{abc} = [i_a \quad i_b \quad i_c]^T$ is the stator phase currents vector; R_s and $L_s = L + M$ are the stator winding resistance and inductance, respectively and $e_{abc} = [e_a \quad e_b \quad e_c]^T$ is the back electromotive force (EMF) due to the rotor movement and can be given by

$$e_{abc} = M_f i_f \omega \widetilde{\sin}\theta \tag{2}$$

where $M_f i_f$ is the flux field; ω is the speed; θ is the rotor angle and

$$\widetilde{\sin}\theta = [sin\theta \quad sin(\theta - \frac{2\pi}{3}) \quad sin(\theta + \frac{2\pi}{3})].$$

The mechanical part of the machine can be written by

$$J\dot{\omega}_g = T_m - T_e - D_p\omega \tag{3}$$

where J is the moment of inertia of all the parts rotating with rotor; T_m is the mechanical torque; T_e is the electromagnetic torque and D_p is a damping factor. The electromagnetic torque, T_e can be found from the energy stored in the magnetic field of the machine and can be given by

$$T_e = M_f i_f \left\langle i_{abc}, \widetilde{\sin}\theta \right\rangle \tag{4}$$

where $\langle \cdot, \cdot \rangle$ denotes the conventional inner product between two matrices in $\mathbb{R}^3$. The active and reactive powers, denoted P and Q respectively, generated by an SG can be given as

$$P = M_f i_f \omega \left\langle i_{abc}, \widetilde{\sin\theta} \right\rangle \tag{5}$$

$$Q = -M_f i_f \omega \left\langle i_{abc}, \widetilde{cos\theta} \right\rangle . \tag{6}$$

The synchronverter concept is developed based on the SG model (1)-(6).

The swing equation for the grid-side synchronverter can be given in (7) where the mechanical torque, T_m is a control input obtained through the maximum power point tracking (MPPT) algorithm as described by Ma et al [6] and the electrical torque, T_e depends on i_{abc} and θ_g according to (4). To have similar behaviour as an SG, a frequency droop control loop is included, hence, the swing equation of the grid side-converter can be given by

$$J\dot{\omega}_g = P_{ref,MPPT}/\omega_n - T_e - D_p(\omega - \omega_n) \tag{7}$$

where $P_{ref,MPPT}$ is reference active power obtained through the MPPT algorithm [6].

The electrical circuit of the grid-side WECS inverter including the synchronverter controller is given in Fig. 1. The voltage in (2) corresponds to the back EMF of the virtual rotor. The inverter switches are operated such that over a switching period, the converter outputs are to be equal to e_{abc} as given in (2) and it is achieved by a PWM technique.

In order to regulate the field excitation, $M_f i_f$, the reactive power is controlled by a voltage droop control loop using voltage droop coefficient, D_q. The control of reactive power is shown in the lower part of Fig. 1 where the inner loop is the voltage (amplitude) loop and outer loop is the reactive power loop. The magnetic field excitation, $M_f i_f$ and reactive power reference, Q_{ref} can be given by

$$M_f i_f = \frac{1}{K_q s}(Q_{ref} - Q + D_q(V_{m,g} - V_{m,pcc}) \tag{8}$$

where $V_{m,pcc}$ is the output voltage magnitude and $V_{m,g}$ is the reference voltage magnitude.

The control structure of the grid side controller is depicted to the right in Fig. 1, where the active and reactive drooping coefficients are denoted D_p and D_q respectively. The structure is modified from Ma et al [23] and utilizes the inherent synchronization ability of the synchronous machine to achieve self-synchronization with the grid. The main objective of the grid side inverter is to feed the correct amount of power into the grid, based on the MPPT of the turbine, frequency- and voltage situation of the grid.

2.2 Control of rotor-side converter

Controlling a three-phase rectifier as a Synchronverter was first proposed by Ma et al [26], and later added with the self-synchronization ability [24]. The control structure of the rotor side controller is depicted to the left in Fig. 1 and is modified from Ma et al [26]. Here the active drooping coefficient is denoted D_{pm}, and the core of the rotor side rectifier controller is the same as for the grid side, however now with the converter current defined in the opposite direction. The main objective of the rotor side rectifier is to keep the DC link voltage at its reference voltage and at the same time keep the power factor at the rotor side as close to unity as possible.

The swing equation for the rotor-side synchronverter can be given by

$$J_m\dot{\omega} = T_m - T_e - D_{pm}(\omega - \omega_e) \tag{9}$$

where ω_e is the frequency of the generated voltage of the PMSG. The mechanical torque, T_m is the control input. Hence, the WECS dc-link voltage can be controlled by controlling the mechanical torque and it is generated by PI-controller as shown in Fig. 1 and can be given by

$$T_m = (K_{p,dc} + \frac{K_{i,dc}}{s})(V_{DC} - V_{DC,ref}) \tag{10}$$

where $K_{p,dc}$ and $K_{i,dc}$ are the proportional and integral gain of the dc voltage controller, respectively.

3 Small-signal modeling and tuning of the control-loops

The control structure presented in Fig. 1 can now be used to develop a small-signal model, yielding the block diagrams of the Synchronverter for both the grid-side converter and rotor side converter control.

3.1 Grid-side synchronverter

The converter controller consist of two control channels; one for the active power and one for the reactive power. Therefore the first objective is to find the transfer function from the active power reference P_{ref} to the actual power P, and the transfer function from the reactive power reference Q_{ref} to the actual power Q. It is known that for a grid-connected synchronous machine the powers can be calculated as

$$P = \frac{3V_{pcc}V_g}{X_s}\sin\delta \tag{11a}$$

$$Q = \frac{3(V_{pcc} - V_g\cos\delta)V_{pcc}}{X_s} \tag{11b}$$

where the parameters used are related to the Synchronverter, and it is assumed that the grid impedance $Z_g = R_g + jX_s$ is mainly inductive, i.e. $X_s = \omega_n L_g >> R_g$. Using $v_g = V_g\angle 0°$ implies $\delta = \theta - \theta_g = \theta$, i.e. the power angle of the system is the angle of the PCC voltage.

To develop the small-signal model, the variables are defined as

$$x = x_n + \Delta x \tag{12}$$

where x_n denotes the nominal value, while the small deviation is denoted Δx. It can be assumed $\Delta V_g = 0$ and $\Delta\omega_g = 0$ when developing the small-signal model. Applying the approximations $sin\delta_n \approx \delta_n$, $sin\Delta\delta \approx \Delta\delta$, $cos\delta_n \approx 1$ and $cos\Delta\delta \approx 1$, and in addition neglect the constant terms and higher order varying terms, (11a) and (11b) can be rewritten into the Laplace domain as in (13a) and (13b) [11].

$$\Delta P = \frac{3V_{pcc,n}V_{gn}}{X_s}\Delta\delta(s) + \frac{3V_{gn}\delta_n}{X_s}\Delta V_{pcc}(s) \tag{13a}$$

$$\Delta Q = \frac{3V_{pcc,n}}{X_s}\Delta V_{pcc}(s) + \frac{3V_{pcc,n}V_{gn}\delta_n}{X_s}\Delta\delta(s) \tag{13b}$$

Further, using the approximation that the small signal feedback voltage amplitude is approximately equal to the small signal back-emf amplitude, i.e. $\Delta V_{pcc} \approx \Delta E$, and equations (13a) and (13b), the control system from the grid side in figure 1 can be presented in block diagram as shown in figure 2. Note that for the block diagrams the definitions $K_p = \frac{1}{J}$ and $K_{qi} = \frac{1}{K_q}$ are used.

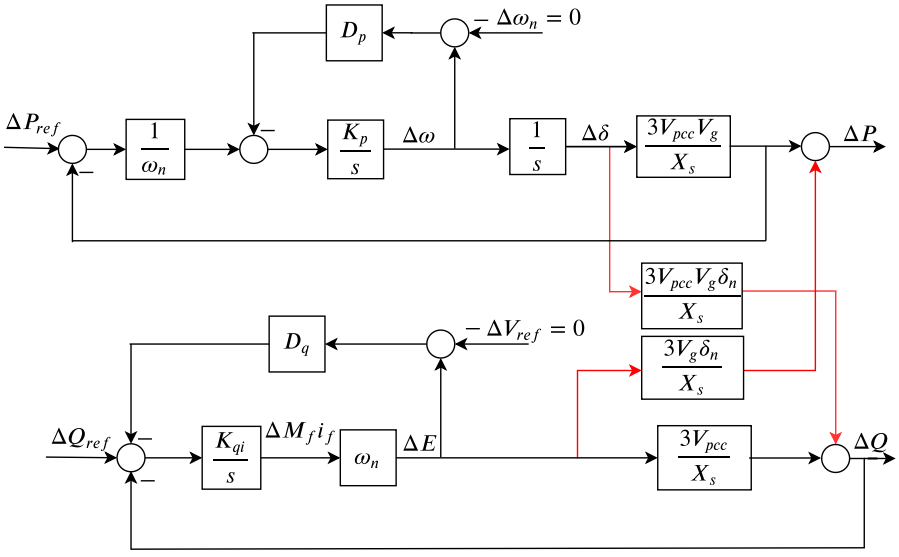

Figure 2: Block diagram of the coupled grid side control system.

As can be seen from both the block diagram and the small-signal power equations the active power loop (APL) and reactive power loop (RPL) are coupled. The coupling is coming from (13a) and (13b) where both ΔP and ΔQ are depending on $\Delta\delta$ coming from the APL and $\Delta V_{pcc} = \Delta E$ coming from the RPL. The loops must therefore be de-coupled to simplify the system analysis.

If the coupling is omitted the two loops can be simplified as in figures 3 and 4, from which the two open loop gains $T_{APL,grid}$ and $T_{RPL,grid}$ can be easily identified in (14a) and (14b).

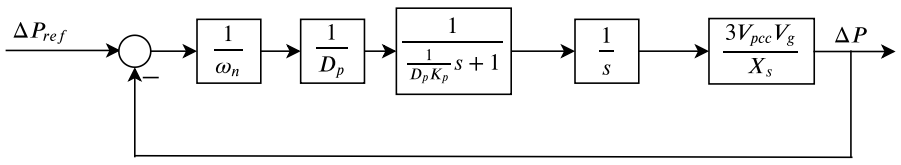

Figure 3: Simplified block diagram of the grid side APL when coupling is omitted.

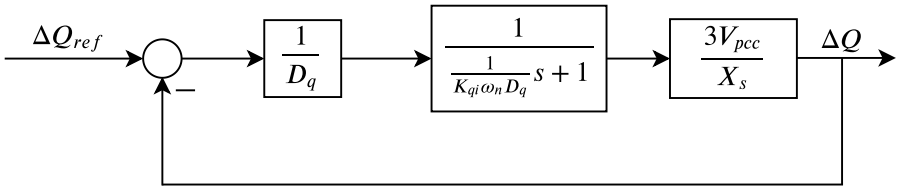

Figure 4: Simplified block diagram of the grid side RPL when coupling is omitted.

$$T_p(s) = \frac{1}{\omega_n} \cdot \frac{1}{D_p} \cdot \frac{1}{\frac{1}{D_p K_p}s+1} \cdot \frac{1}{s} \cdot \frac{3V_{pcc,n}V_{gn}}{X_s} \tag{14a}$$

$$T_q(s) = \frac{1}{D_q} \cdot \frac{1}{\frac{1}{K_{qi}\omega_n D_q}s+1} \cdot \frac{3V_{pcc,n}}{X_s}. \tag{14b}$$

Now, by setting ΔQ to zero in Fig. 2, it can be shown that the loop gain of the APL including the coupling will be

$$T_{pc}(s) = T_p(s)\Big(1 - \frac{T_q(s)}{1+T_q(s)}\delta_n^2\Big). \tag{15}$$

Similarly, by setting ΔP to zero in figure 2, it can be shown that the loop gain of the RPL including the coupling will be

$$T_{qc}(s) = T_q(s)\Big(1 - \frac{T_p(s)}{1+T_p(s)}\delta_n^2\Big). \tag{16}$$

The APL and RPL, in the upper and lower part of Fig. 2, are coupled due to the inherent nature of the VSM, as both and P and Q are related to V and δ. This coupling brings difficulty to parameter design. For simplification of the tuning procedure, the loops can be considered decoupled [11] which simplifies to

$$T_{pc} \approx T_p$$

$$T_{qc} \approx T_q$$

and the controller parameters can therefore be designed separately for the active power loop and reactive power loop from the decoupled structure.

3.1.1 Active Power Loop

The parameters for the APL can now be tuned based on the transfer function given in (14). As seen in Fig. 3 there are essentially two parameters that needs to be tuned in the APL; D_p and K_p. The drooping coefficients are often treated as a result of grid code requirements, where a 100% change in active or reactive power is required for a certain amount of change in frequency or voltage respectively. Therefore using a pre-selected drooping percentage $\Delta p\%$ the droop coefficient D_p can be set as

$$D_p = \frac{\frac{P_n}{\omega_n}}{\omega_n \cdot \Delta p_{\%}} \tag{17}$$

The next parameter is $K_p = \frac{1}{J}$. It is known that the amplitude of the open loop APL gain is unity at the gain crossover frequency and this can be used to express K_p as a function of the crossover frequency f_{pc}. The magnitude of the transfer function at crossover can be given by

$$|T_p(j2\pi f_{pc})| = \frac{3V_{pcc,n}V_{gn}}{X_s\omega_n D_p} \frac{1}{\left|\frac{j2\pi f_{pc}}{D_p K_p}+1\right|} \frac{1}{|j2\pi f_{pc}|} = 1$$

which gives the value of K_p as

$$K_p = \frac{2\pi f_{pc}}{D_p\sqrt{\left(\frac{3V_{pcc,n}V_{gn}}{2\pi f_{pc}X_s\omega_n D_p}\right)^2 - 1}} \tag{18}$$

It is, in addition to optimise stability and controller performance, important to attenuate the Double Line-Frequency Ripples (DLFR) in the output voltage caused by the instantaneous power outputs during periods of unbalanced grid voltages. To ensure that the DLFR is attenuated properly the magnitude of the loop gain should also be assessed at the the frequency $2f_n$, i.e.:

$$|T_p(j2\pi \cdot 2f_n)| = \frac{3V_{pcc,n}V_{gn}}{X_s\omega_n D_p} \cdot \frac{1}{\left|\frac{j4\pi f_n}{D_p K_p} + 1\right|} \cdot \frac{1}{|j4\pi f_n|}$$

This expression can be simplified using the approximation

$$\frac{1}{\left|\frac{j4\pi f_n}{D_p K_p} + 1\right|} \approx \frac{1}{\left|\frac{j4\pi f_n}{D_p K_p}\right|}$$

due to the fact that the cutoff frequency $\frac{D_p K_p}{2\pi}$ of the first order filter in T_p is way below $2f_n$, yielding

$$|T_p(j2\pi \cdot 2f_n)| \approx \frac{3V_{pcc,n}V_{gn}K_p}{16\pi^2 f_n^2 X_s\omega_n} \leq a_p \tag{19}$$

where a_p is the maximum desired magnitude at $f = 2f_n$. The criteria in (20) can thus be found using (19).

$$K_p \leq \frac{16\pi^2 f_n^2 X_s\omega_n a_p}{3V_{pcc,n}V_{gn}} = K_{p,max} \tag{20}$$

To ensure a robust controller with good stability, the phase margin should also be taken into consideration when tuning the parameters. The desired phase margin for the open-loop gain is defined as $PM_{desired}$, yielding the criteria in (21).

$$PM = 180° + \angle T_{APL,grid}(j2\pi f_{pc}) \geq PM_{desired} \tag{21}$$

The part of (14a) governing the angle will be

$$\frac{1}{\frac{1}{D_p K_p}s + 1} \cdot \frac{1}{s}$$

where $\frac{1}{s}$ automatically translate to $-90°$, yielding

$$90° - \arctan\frac{\Im(\frac{1}{D_p K_p}j2\pi f_{pc} + 1)}{\Re(\frac{1}{D_p K_p}j2\pi f_{pc} + 1)} = 90° - \arctan\frac{\frac{2\pi f_{pc}}{D_p K_p}}{1}$$

The angle should be larger, or equal, to the desired phase margin, i.e. $\geq PM_{desired}$. Based on the above the minimum value of K_p can thus be calculated in (22).

$$K_p \geq \frac{2\pi f_{pc}}{D_p}\tan(PM_{desired}) = K_{p,min} \tag{22}$$

Using (18), (20) and (22), $K_{p,min}$, $K_{p,max}$ and K_p can be plotted as functions of the crossover frequency f_{pc}, and any value of $K_p(f_{pc})$ lying within the two curves $K_{p,min}$ and $K_{p,max}$ will satisfy the tuning criteria for the APL. It is usually beneficial to chose the value for K_p in the higher area of the valid range to improve controller performance to have a faster response in response to a disturbance.

3.1.2 Reactive Power Loop

From Fig. 4 it can be deduced that there are two parameters that should be designed for the RPL; D_q and K_{qi}. As for the drooping coefficient of the APL, the drooping coefficient of the RPL will be a result of grid code requirements. Using a drooping percentage $\Delta q\%$ the droop coefficient D_q can be set as:

$$D_q = \frac{Q_n}{\sqrt{2}V_{gn,L-G} \cdot \Delta q\%}. \tag{23}$$

The final parameter to be decided for the grid side controller is $K_{qi} = \frac{1}{K_q}$, and the tuning procedure will be similar as for K_p. From the loop gain in (14b) it can be seen that the denominator only consist of s to the power of 1, i.e. its a first order denominator. This implies that the phase of the RPL reaches a minimum of $-90°$ and thus the phase margin will always be 90° or more, meaning no lower limit for K_{qi} is needed. As was the case for the APL the DLFR must be attenuated properly also for the RPL, creating the need to assess the magnitude of the loop gain at the the frequency $f = 2f_n$, i.e.:

$$|T_q(j2\pi \cdot 2f_n)| = \frac{3V_{pcc,n}}{D_q X_s} \cdot \frac{1}{\left|\frac{j4\pi f_n}{D_q K_{qi}\omega_n} + 1\right|}$$

which can be simplified using the approximation

$$\frac{1}{\left|\frac{j4\pi f_n}{D_q K_{qi}\omega_n} + 1\right|} \approx \frac{1}{\left|\frac{j4\pi f_n}{D_q K_{qi}\omega_n}\right|}$$

as the cutoff frequency $\frac{D_q K_{qi}\omega_n}{2\pi}$ of the first order filter in $T_{RPL,grid}$ is way below $2f_n$, yielding

$$|T_q(j2\pi \cdot 2f_n)| \approx \frac{3V_{pcc,n}K_{qi}\omega_n}{4\pi f_n X_s} \leq a_q$$

where a_q is the maximum desired magnitude at $f = 2f_n$. The criteria in (24) can thus be found using the relation above.

$$K_{qi} \leq \frac{4\pi f_n X_s a_q}{3V_{pcc,n}\omega_n} = K_{qi,max} \tag{24}$$

3.2 Small-signal modeling of the rotor-side Synchronverter

The rotor-side synchronverter also consists of two control channels; one for the dc voltage control and one for the reactive power control. It is therefore necessary to find the transfer function from the DC voltage reference $V_{DC,ref}$ to the actual voltage V_{DC}, and the transfer function from the reactive power reference Q_{ref} to the actual power Q. Also for the rotor side rectifier controller, a small signal model will be used, and as the method of de-coupling the APL and RPL will be very much the same as for the grid side controller, the procedure will not be repeated here.

The inner loops of the rectifier upper control channel are essentially identical to the grid side APL, with the only difference being that the active power will be negative. For the outer DC voltage loop, the mechanical torque will be created by the PI controller. To find the outer loop in the small-signal model, the deviations around the steady-state values are defined in (25a) and (25b). The objective is here to find the transfer function from ΔP to ΔV_{DC}.

$$V_{DC} = V_{DC,n} + \Delta V_{DC} \tag{25a}$$

$$I_{DC} = I_{n,DC} + \Delta I_{DC} \tag{25b}$$

Using the nominal plus the small signal values of P, (25a) and (25b) can be used to yield the following result:

$$P_n + \Delta P = (V_{DC,n} + \Delta V_{DC})(I_{n,DC} + \Delta I_{DC}) \tag{26}$$

When ignoring the DC term, the second order term, and applying the approximation $\Delta I \approx 0$ the transfer function from ΔP to ΔV_{DC} can be found in (27b) based on (27a).

$$\Delta P = \Delta V_{DC} I_{n,DC} \Longrightarrow \Delta V_{DC} = \frac{\Delta P}{I_{n,DC}} \tag{27a}$$

$$H_{P-V_{DC}} = \frac{1}{I_{n,DC}} \tag{27b}$$

Using the transfer function above, and the fact that the active power will be negative, the rotor-side control system can be presented in the small-signal form through block diagrams as shown in figures 5 and 6 for the DC voltage control and reactive power control channels respectively. Note that they are assumed to already be de-coupled, and that the definitions $K_{pm} = \frac{1}{J_m}$ and $K_{qi,m} = \frac{1}{K_{qm}}$ are used.

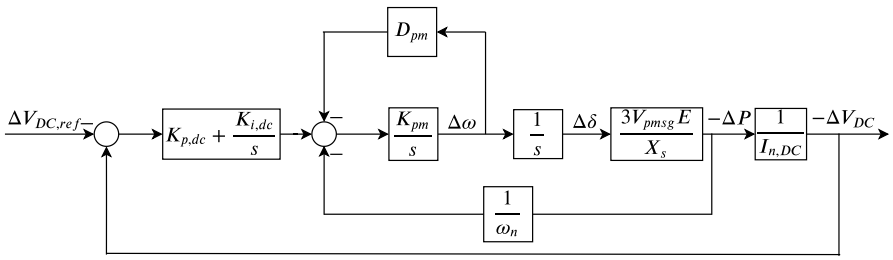

Figure 5: Block diagram of the upper control channel for a Synchronverter based rectifier control system.

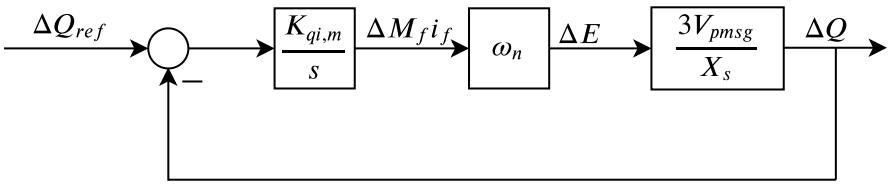

Figure 6: Block diagram of the lower control channel for a Synchronverter based rectifier control system.

As seen in Fig. 5 the block diagram is not represented in its standard form as the reference is coming in negative and the feedback is positive. For simplified system analysis, the fact that ΔP is negative can be taken advantage of by multiplying the loop gain with minus one, essentially switching the signs of both the feedback and reference and at the same time obtaining a positive ΔV_{DC}. This yields the simplified version of the block diagram representing the upper control channel in Fig. 7.

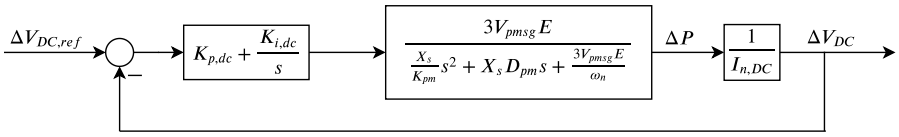

Figure 7: Simplified upper control channel block diagram on standard form.

From figures 7 and 6 the two open loop gains $T_{DC,rotor}$ and $T_{RPL,rotor}$ can be easily identified in (28) and (29).

$$T_{DC} = (K_{p,dc} + \frac{K_{i,dc}}{s}) \cdot \Big(\frac{3V_{pmsg}E}{\frac{X_s}{K_{pm}}s^2 + X_s D_{pm} s + \frac{3V_{pmsg}E}{\omega_n}} \Big) \cdot \frac{1}{I_{n,DC}} = G \cdot H \tag{28}$$

$$T_{q,r} = \frac{K_{qi,m}}{s} \cdot \omega_n \cdot \frac{3V_{pmsg}}{X_s} \tag{29}$$

In (28), G and H are defined as

$$G = (K_{p,dc} + \frac{K_{i,dc}}{s})$$

$$H = \Big(\frac{3V_{pmsg}E}{\frac{X_s}{K_{pm}}s^2 + X_s D_{pm} s + \frac{3V_{pmsg}E}{\omega_n}} \cdot \frac{1}{I_{n,DC}} \Big)$$

3.2.1 Tuning the DC voltage PI Controller

D_{pm} has the exact same definition as D_p and thus does not need to be re-tuned for the rotor side. For simplicity reasons and to limit the scope of this research, the parameters K_{pm} and $K_{qi,m}$ are set equal to their grid side counterparts K_p and K_{qi}. The RPL of the rotor side controller has thus no further parameters that need to be decided, and the focus can be shifted to the DC voltage control loop.

Here, only the parameters for the PI controller creating the reference torque based on the DC voltage deviation needs to be designed. Different methods can be applied to tune a PI controller, and many of them are essentially different methods of applying the *trial and error* method. One example of such a method is the process of

selecting a crossover frequency ω_c and then use the trial and error method to chose the proportional gain $K_{p,dc}$ and the integral gain $K_{i,dc}$ such that the amplitude of the loop gain at the selected crossover frequency is unity, i.e.

$$|T_{DC,rotor}(j\omega_c)| = 1$$

Another trial and error method is to use the step response of the closed-loop system, in combination with a Bode diagram of the open-loop gain, to find parameters that yield both a fast and precise response and have acceptable stability margins. However, the procedures using the trial and error method are inherently time-consuming and provides no guarantee of finding the parameters yielding the best possible controller performance. It is therefore beneficial to find a starting point close to the optimal parameters by use of a faster and more precise tuning procedure so that any additional use of the trial and error method will be limited to a minimum.

The idea will be to set the closed-loop transfer function approximately equal to a first-order filter. The open-loop gain of the DC voltage control loop is given in (28) and by closing the loop with a feedback gain equal to 1, the closed-loop can be found as:

$$\frac{G \cdot H}{1 + G \cdot H}$$

Setting the closed-loop equal to a first-order low-pass filter as

$$\frac{G \cdot H}{1 + G \cdot H} = \frac{\alpha}{s + \alpha} \tag{30}$$

where α is the corner frequency of the first order filter, also known as the bandwidth. From (30) it can be derived that

$$G \cdot H \approx \frac{\alpha}{s}$$

which yields the relation seen in (31).

$$(K_{p,dc} + \frac{K_{i,dc}}{s}) \cdot \left(\frac{3V_{pmsg}E}{\frac{X_s I_{n,DC}}{K_{pm}} s^2 + X_s I_{n,DC} D_{pm} s + \frac{3V_{pmsg} E I_{n,DC}}{\omega_n}} \right) \approx \frac{\alpha}{s} \tag{31}$$

Using (31) and applying mathematical derivations, (32) is obtained.

$$(K_{p,dc} + \frac{K_{i,dc}}{s}) \approx \alpha \frac{X_s I_{n,DC}}{3V_{pmsg}EK_{pm}} s + \alpha \frac{X_s I_{n,DC} D_{pm}}{3V_{pmsg}E} + \alpha \frac{I_{n,DC}}{\omega_n s} \tag{32}$$

It can quickly be deduced that as the controller used is a PI controller and not a PID controller, i.e. G does not have a derivative part, the fraction multiplied with s in (32) must be set to zero. This approximation will have an impact on the design process as will be discussed later. Neglecting the derivative part and comparing the two sides of (32) the desired gains can be approximated in (33a) and (33b).

$$K_{p,dc} = \alpha \frac{X_s I_{n,DC} D_{pm}}{3V_{pmsg}E} \tag{33a}$$

$$K_{i,dc} = \alpha \frac{I_{n,DC}}{\omega_n} \tag{33b}$$

Now, by selecting a corner frequency α yielding an acceptable bandwidth, the above-calculated controller gains can be used as a starting point for further manual tuning using the trial and error method. Since the procedure above is based on approximations, the bandwidth of the actual control loop will not necessarily be equal to α. It is therefore important to apply manual tuning after obtaining the initial parameters to ensure that both the bandwidth and phase margin are acceptable.

4 Tuning example

Before simulations can be carried out, the controller parameters need to be designed based on the outlined tuning method. The final controller parameters are found in Table 1, while the system parameters used in the tuning procedure are listed in Table 2.

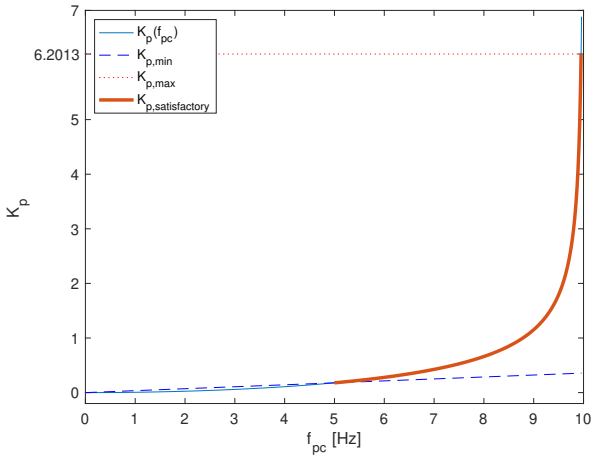

Figure 8: Plot showing valid range of K_p.

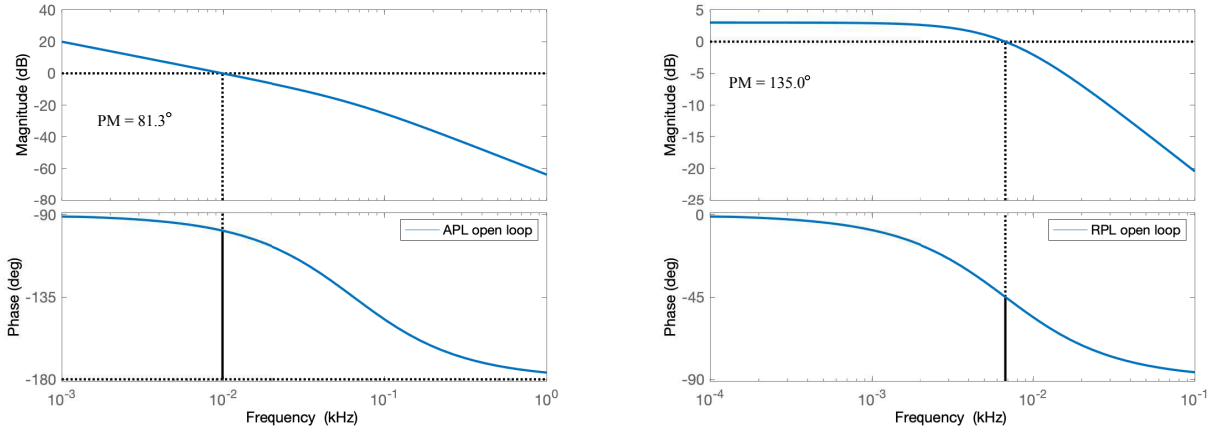

(a) Open loop APL.

(b) Open loop RPL.

Figure 9: Bode plots for grid side controller.

First, $D_p = D_{pm}$ and D_q are set using (17) and (23), resulting in (34a) and (34b). For the purpose of this paper the grid code requirements from the standard EN50438 will be used, meaning $p_{change,\%} = 2\%$ and $p_{change,\%} = 10\%$ [11].

$$D_p = D_{pm} = \frac{\frac{200kW}{2\pi \cdot 50}}{2\pi \cdot 50 \cdot 0.02} = 101.3212 \tag{34a}$$

$$D_q = \frac{200kVAr}{\sqrt{\frac{2}{3}} \cdot 690 \cdot 0.1} = 3550 \tag{34b}$$

Next, $K_p = K_{pm}$ are to be determined. Here, a maximum magnitude at double the line frequency, $a_p = 0.1$ and $a_q = 0.1$ will be used. Equations (18), (20) and (22) along with the simplifications that $V_{pcc} \approx V_g$ and $E \approx V_{pmsg}$, can then be utilised to obtain Fig. 8. From Fig. 8 a value of K_p can be chosen in the higher area of the satisfactory curve, and here $K_p = 4$ is chosen. The controller parameter $J = J_m$ can then be calculated as

$$J = J_m = \frac{1}{K_p} = 0.25 \tag{35}$$

K_{qi} is chosen close to $K_{qi,max} = 3.9837 \cdot 10^{-5}$ calculated from (24), and is thus chosen to be $K_{qi} = 3.8 \cdot 10^{-5}$. The controller parameters $K_q = K_{qm}$ is then calculated as:

$$K_q = K_{qm} = \frac{1}{K_{qi}} = 26316 \tag{36}$$

Bode plots of the APL and RPL of the grid side controller are depicted in figures 9a and 9b respectively.

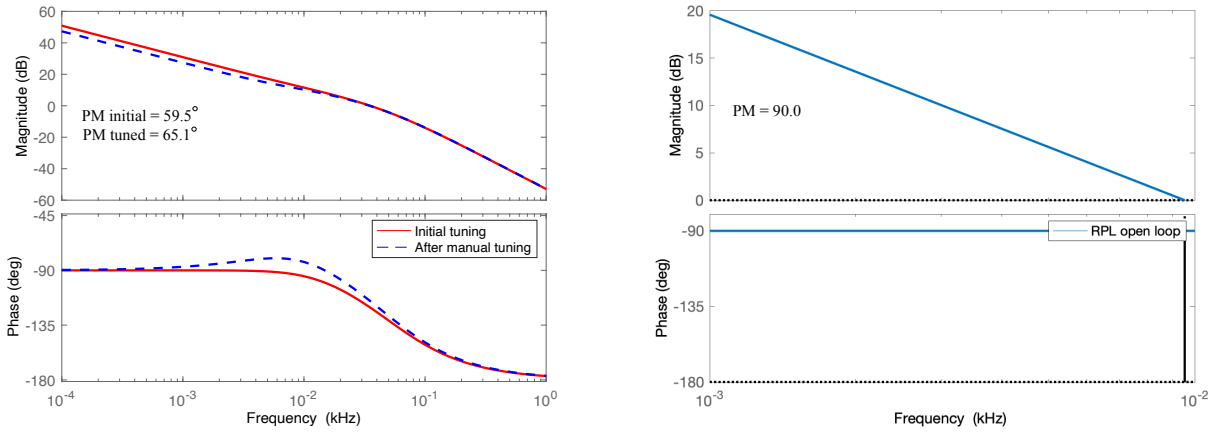

(a) DC voltage open loop.

(b) Open loop RPL.

Figure 10: Bode plots for rotor side controller.

As seen from Fig. 9a and 9b the magnitude at double the line frequency, i.e. 100 Hz, is indeed found to be $-20dB$, and thus the criteria of $a_p = 0.1$ and $a_q = 0.1$ is achieved.

Finally, the parameters of the PI controller needs to be tuned. Equations (33a) and (33b) are used to obtain initial values for $K_{p,dc}$ and $K_{i,dc}$. In these initial calculations α is set to $\alpha = 220$ rad/s $\approx$ 35Hz, resulting in $K_{p,dc} = 1.9783 \approx 2.0$ and $K_{i,dc} = 124.2995 \approx 124.3$. Using these initial values the phase margin of the open-loop is found to be below 60°, and the bandwidth of the closed-loop is be found to be $56.29\,Hz$. A common rule of thumb for bandwidth is that the bandwidth of the most inner loop should be 3-10 times lower than the switching frequency and then 3-10 times lower for the next loop etc. Looking at Fig. 5, the DC voltage loop is the third loop after the frequency loop and power loop. Therefore using the rule of thumb, a bandwidth of 56 Hz is just within the recommended range, and thus deemed as acceptable for now. In this paper, a minimum phase margin of 65° is desired for stability, and therefore additional tuning must be applied.

Two options arises to improve stability; decrease the proportional gain or decrease the integral gain. First $K_{p,dc}$ is decreased to $K_{p,dc} = 1.5$, while $K_{i,dc}$ is kept unchanged, resulting in a system where the phase margin is approximately unchanged, while the bandwidth is found to have decreased to $46.40\,Hz$. Therefore, the next step is to try to decrease $K_{i,dc}$ to $K_{i,dc} = 100$, while keeping $K_{p,dc}$ unchanged from the initial value. This yields a system with an improved phase margin equal to 62.8°, while the bandwidth is found to be approximately the same at $55.06\,Hz$.

Based on these results additional tuning is applied by further decreasing $K_{i,dc}$, ultimately yielding the final controller parameters $K_{p,dc} = 2.0$ and $K_{i,dc} = 82.5$. The Bode plot of the open loop DC voltage loop with the final parameters is depicted in Fig. 10a, where it is also compared to the the Bode plot using the initial values. The phase margin is 65.1° and the bandwidth of the closed loop is found to be $54.61\,Hz$. In addition, the Bode plot of the RPL of the rotor side is depicted in Fig. 10b, and the controller parameters are provided in Table 1.

Table 1: Controller Parameters.

Parameter	**Value**	**Parameter**	**Value**
$J = J_m$	0.25	$K_q = K_{qm}$	26316
$D_p = D_{pm}$	101.3212	D_q	3550
$K_{p,dc}$	2.0	$K_{i,dc}$	82.5

5 Simulation Results

In order to show the effectiveness and functioning of the tuned control parameters, simulations have been carried out using MATLAB/Simulink association with SimPower System tool box. The investigated synchronverter-based WECS is shown in figure 1 which consist of a wind turbine rated at 200 kW. The rated voltage of both the PMSG and the infinite bus is $690V$ line to line with gird frequency $50Hz$ and the DC link voltage is $1126.8V$.

The simulations were carried out using the fixed step solver *ode3* with a sample time $T_s = 1 \cdot 10^{-6}s = 1\mu s$. The plots depicting the response of the rotor side controller are shown in Fig. 11, while the plots depicting the

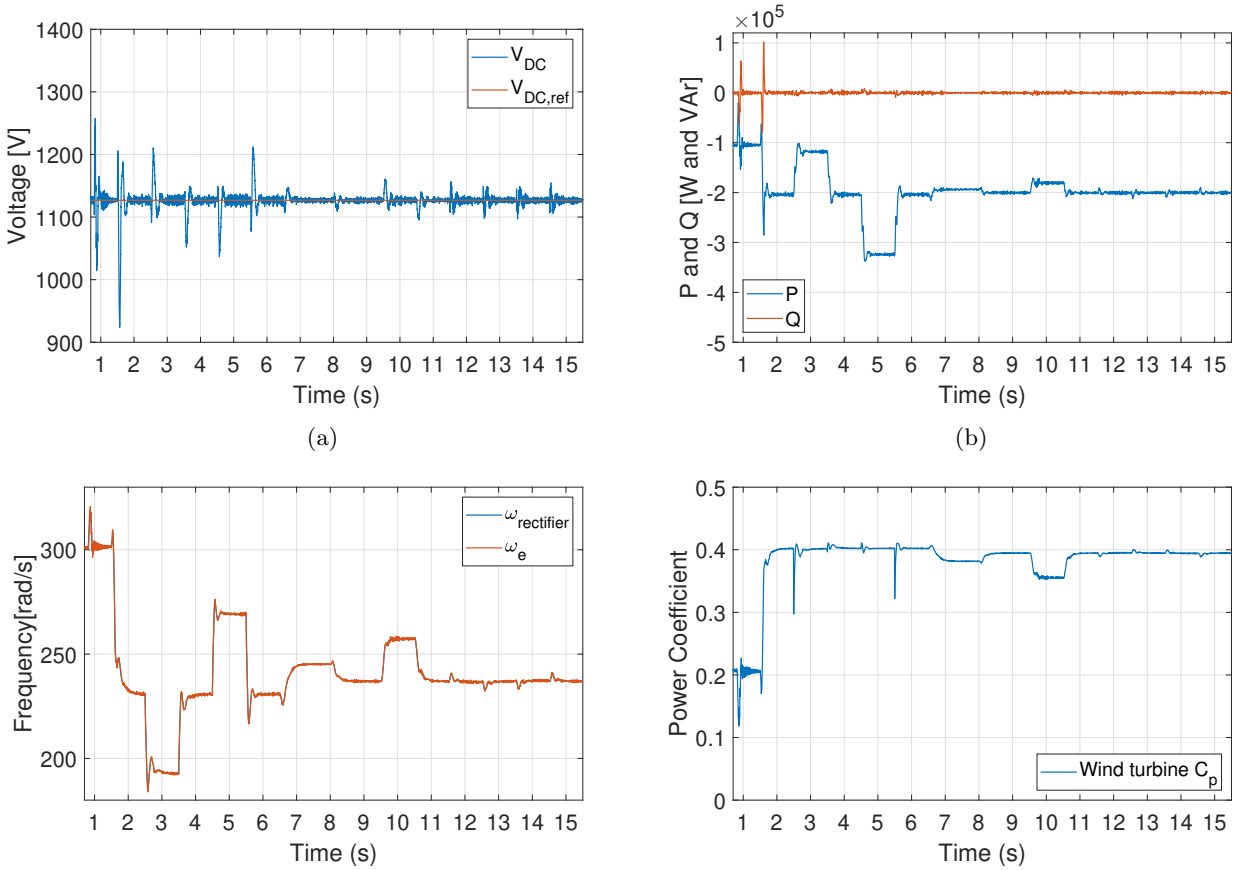

Figure 11: Rotor Side Simulation Results: (a) DC link voltage, (b) Powers calculated by the rectifier, (c) Rectifier frequency vs PMSG stator frequency and (d) Power coefficient of the wind turbine.

response of the grid side controller are shown in Fig. 12. Figure 13 shows the transient response of the DC-link voltage and the active and reactive power. Note that the first 0.7 seconds representing the synchronisation period is omitted from the plots. The simulation has the following sequence of events:

1. The simulation was started at $t = 0$ with all IGBTs off and the circuit breaker in the open position. The initial wind speed is $12\,m/s$. In the DC link a resistance equal to $2 \cdot R_{chopper}$ was connected to obtain the DC voltage, and the virtual synchronisation currents were fed to the controllers. The IGBTs on the rotor side was started at $t = 0.2$ with $V_{DC,ref} = 1126.8\,V$ and $Q_{ref,rotor} = 0$. Switch A in the rotor side controller was turned to position 2 to feed the real current to the controller.
2. The IGBTs on the grid side was started at $t = 0.5$ with $P_{ref} = Q_{ref} = 0$, and the voltage droop disabled, i.e. switch B open. Switch A in the grid side controller was turned to position 2 to feed the real current to the controller.
3. The circuit breaker was closed at $t = 0.8$ connecting the grid side converter to the grid. P_{ref} was changed to reflect the MPPT at $t = 1.5$, and the chopper resistance was disconnected to send all available power to the grid side.
4. The wind speed was changed to $10\,m/s$ at $t = 2.5$, to $12\,m/s$ at $t = 3.5$, to $14\,m/s$ at $t = 4.5$, and to $12\,m/s$ at $t = 5.5$
5. $Q_{ref,grid}$ was changed to $100\,kVAr$ at $t = 6.5$. Switch B was closed at $t = 8.0$, enabling the voltage droop loop of the grid side.
6. Grid frequency increase by 0.1 Hz from $t = 9.5$ to $t = 10.5$. Grid voltage decrease by 0.05 p.u. from $t = 11.5$ to $t = 12.5$ and increase by 0.05 p.u. from $t = 13.5$ to $t = 14.5$
7. Simulation was ended at $t = 15.5$

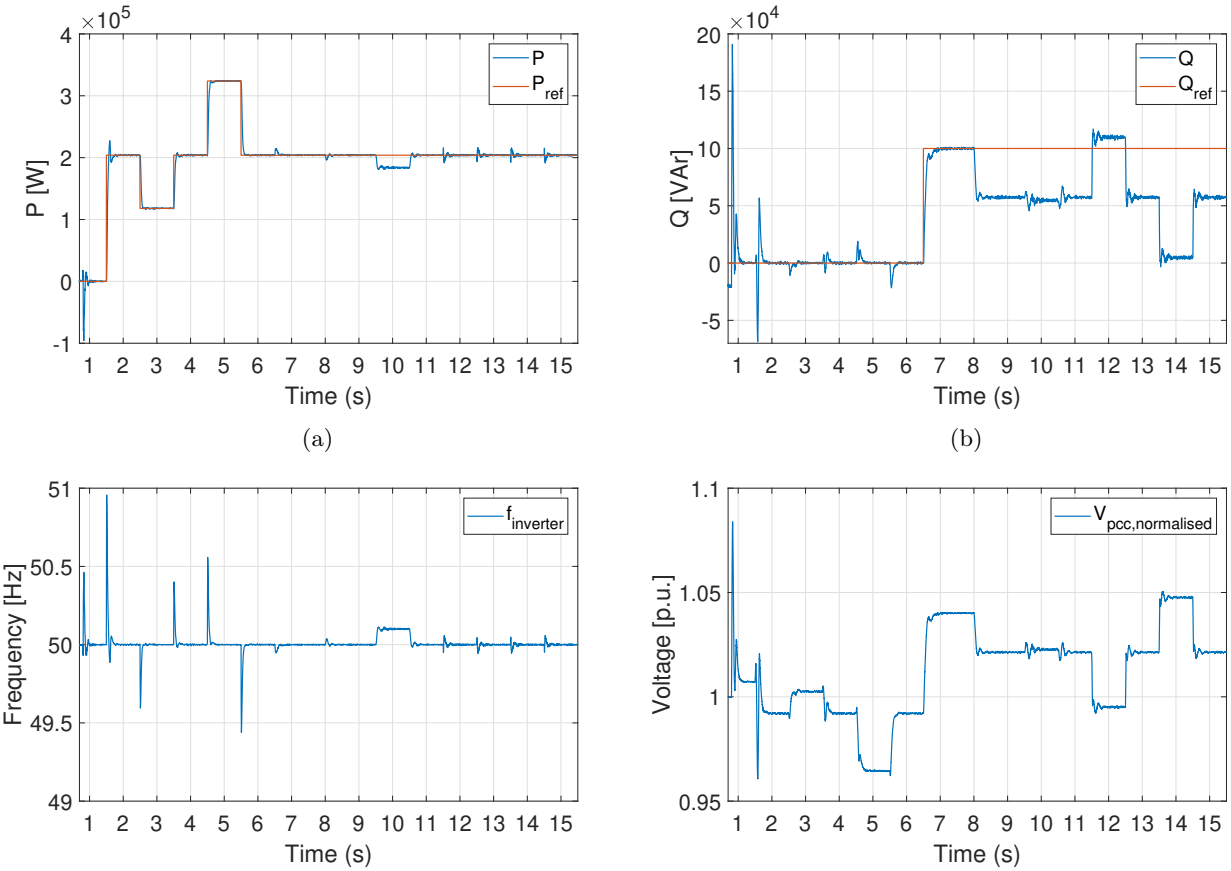

Figure 12: Grid Side Simulation Results: (a) Active power injected by the inverter, (b) Reactive power injected by the inverter, (c) Inverter frequency and (d) Normalised PCC voltage.

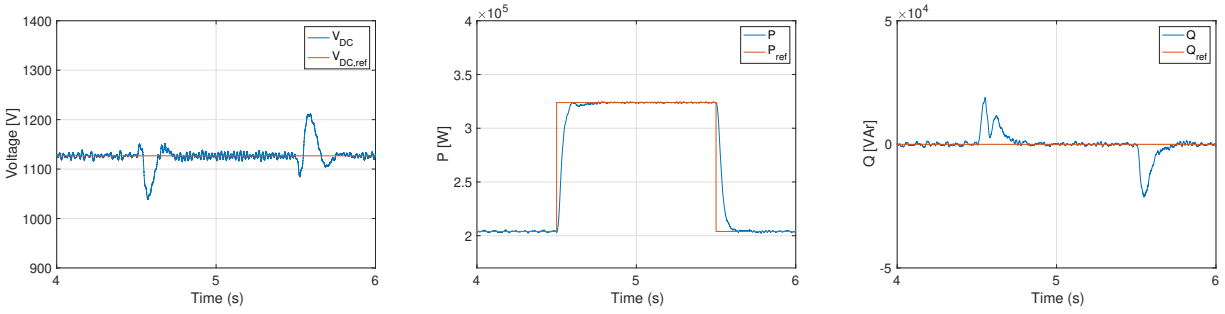

Figure 13: Transient response: (a) DC-link voltage, (b) active power and (c) reactive power of the grid-side converter.

5.1 Performance of the Rotor Side converter

Figure 11a shows the DC link voltage of the WECS. The rotor side controller is able to maintain the DC link voltage at the reference voltage during the entire simulation. Small transients are seen at the occurrence of events, but the controller quickly tracks the reference again after each event. The variations in the DC voltage at steady state vary inside the range from 1100 to 1150 volts, meaning the variation is always less than 50 V in steady state. Fig. Fig. 11b shows the active power and reactive power of the rotor side converter. As can be seen from Fig. 11b, the reactive power was approximately zero during the entire simulation run, meaning the current drawn by the rectifier was in phase with the voltage, and that the desired unity power factor was achieved by the rotor side controller.

Fig. 11c shows the electrical frequency of PMSG and rectifier.As can be seen, the converter speed tracks the electrical speed very well during the entire operation. Figure 11c also shows that the frequency event has a direct impact on the turbine, effectively speeding up the turbine as less power is extracted at the same wind

speed. The voltage events, on the other hand, had very little to zero impact on turbine performance.

These observations are supported by looking at the power coefficient of the turbine in Fig. 11d. It is here clear that the frequency event in A decreased the power coefficient as less power is extracted at the same wind speed, while the power coefficient remains unchanged during the voltage events. Figure 11d also clearly shows that the grid side controller is able to follow the MPPT very closely as the power coefficient of the turbine is very close to the maximum power coefficient $C_{p,max} = 0.411$ during normal operations.

5.2 Performance of the Grid Side converter

Figure 12a depicts the active power injected into the grid by the grid side converter. It is obvious that the power follows the reference very well with very small transients during events. This can also be seen in relation to the high power coefficient as discussed above, and the MPPT-operation is thus achieved by the inverter. The active power is maintained very well also during changes in reactive power injection, and the converter is able to maintain the active power injection also during the voltage events. For the frequency event, i.e. a frequency increase of 0.1 Hz, the frequency droop is working as expected and the converter decreases the power injected into the grid from the MPPT set-point. More specifically, the injected power is decreased by $\approx 20kW = 10\%$ of rated power when the frequency is increased by 0.2%. This change is in line with the designed criteria for the droop; 100% change in active power for 2% change in frequency. When the frequency returns to the rated value, the power injection is increased back to the MPPT set-point.

The reactive power of the grid side converter is shown in Fig. 12b. It can be seen that as long as the voltage droop loop is deactivated, i.e. before switch B is closed at t=8 s, the controller accurately tracks the reference set by the operator. More specifically, as depicted in Fig. 12b, as long as $Q_{ref,grid} = 0$ the reactive power injected is zero at steady state. Small transients can be seen during changes in the active power injection, but the reactive power is quickly controlled back to zero. Also after $Q_{ref,grid}$ was changed at t=6.5 s, the converter quickly controls the injected reactive power to follow the reference. When the voltage droop loop is enabled at $t = 8$, the injected reactive power is reduced from the reference set by the operator as the PCC voltage is higher than the rated voltage. During the voltage events, two opposite control reactions are seen. As expected, when the grid voltage decrease the controller increases the reactive power input to counter the voltage drop in the grid. Opposite, when the grid voltage increase the controller decreases the reactive power input to counter the voltage increase in the grid.

Looking more closely at the results, during the voltage dip the voltage V_{PCC} seen in Fig. 12d decreases from ≈ 1.021 to ≈ 0.995 p.u., i.e. a decrease in the PCC voltage equal to 2.6% of nominal voltage. As seen in Fig. 12b the controller then increases the injected reactive power with approximately 52.5kVAr. This means that there is a change of 52.5kVAr for a change of 2.6% in the voltage. Looking at the designed voltage droop, this is totally in line with expected controller behavior; 100% = 200kVAr change in injected reactive power for 10% change in voltage. The same observations holds for the voltage increase, but with the exact opposite controller reaction, i.e. reducing injected reactive power in accordance with the designed voltage droop.

Also, the grid side converter follows the frequency of the grid which it is connected to very well, as seen in Fig. 12c. Transients are seen during events, but the frequency is quickly controlled back to following the grid frequency. This can be seen also during the frequency increase in A, where the converter frequency has an identical increase. Also, during the voltage events in B and C, the converter is able to track the grid frequency without large deviations.

5.3 Simplifications and Limitations of the Tuning procedure

The simulation model used as well as the tuning procedure proposed in this paper have a number of obvious simplifications and limitations that need to be addressed. It is therefore of interest to discuss the validity of some of the obtained results.

Based on the discussion above it is beyond doubt that the proposed procedure is working, and based on the performance of the control system the controller parameters can be said to be adequately tuned. More specifically, looking at the responses of the DC link voltage and the active and reactive power injections to the grid, their responses are extremely robust while still maintaining stability over the entire operating range. In addition, all references are reached and maintained very well without steady-state deviations when the droop loops are disabled. When activated, both the frequency drooping and voltage drooping works as expected by adjusting the injected active and reactive powers based on the grid conditions, making the controller deviate from pre-set reference set by the operator. From Fig. 11a it can be seen that the DC link voltage is slightly under-dampened with a very fast settling time after the transients occur during events in the simulation. Small oscillations around the voltage reference can be seen, but these are well within the acceptable deviation limit of

5% (a 5% deviation from the DC voltage reference equals a deviation of approximately 56 V). From the grid side results, the active power seems to have a very small overshoot with no further oscillations, while the reactive power is slightly over-dampened when tracking its reference. When the voltage droop activates the response seems to go from slightly over-dampened to slightly under-dampened, resulting in very small oscillations before settling at the reference. The response and settling time are therefore deemed satisfactory.

There are still some factors that should be discussed. Firstly the tuning procedure is based on the line frequency average model using the average powers instead of the instantaneous powers, and the small-signal model used to identify the block diagrams for the control channels will thus not be valid for frequencies high above the nominal frequency. A model that is valid for all frequency ranges could in the future be developed to better accommodate these high frequencies. Secondly, it is possible that the performance of the rectifier could be even better if the simplifications $J_m = J$ and $K_{qm} = K_q$ were avoided. Designing these parameters separately for the rotor side controller instead of putting them equal to their grid side counterparts could help to decrease the fluctuations in the DC link voltage around the reference.

A major simplification is done in the process of tuning the PI controller. More specifically when neglecting the derivative term in (32). The consequence of this simplification can be observed in the bode plot in figure 10a, where the bandwidth of the initial closed-loop is found to be 56.29 Hz instead of the chosen $\alpha = 220$ rad/s ≈ 35 Hz. Based on this it can be deducted that the closed-loop system with parameters that are tuned based on this simplification yields a bandwidth that is higher than the selected α in the tuning process. As a curiosity, the selected 35 Hz is found to be the crossover frequency in this initial Bode plot. Had the controller been a PID controller on the other hand, the derivative gain in the controller could be set equal to the part which is neglected in the simplification, yielding a closed-loop bandwidth actual equal to α. This is however not done as PID controllers tend to be more sensitive against noise and thus less suitable for large industrial applications.

Also, during the tuning procedure, the bandwidth between 50 and 60 Hz for the DC voltage control loop is deemed as acceptable, and no further investigation or tuning steps were done to perfect the bandwidth. In retrospect, a more thorough analysis of the bandwidth should be implemented into the tuning procedure for the PI controller, to ensure controller speed without interference. This adds to the thought that since so many simplifications are made throughout the tuning process, there are a lot of uncertainties related to the stability margins of the system. It can therefore also be discussed if the phase margin of 65° for the DC voltage control loop is actually enough to ensure the stability of the rectifier, as the actual phase margin of the controller could be lower.

6 Conclusions

This paper presents the tuning of a synchronverter based wind energy conversion system. The proposed procedure offers a fast process where system parameters can be easily changed, resulting in new controller parameters without time-consuming calculations. Based on the results and discussion above it can be concluded that the established tuning procedure has shown to yield a well-functioning control system with fast and accurate responses, thus achieving the desired functioning. Simulation results are presented to show the effectiveness of the proposed tuning. It is shown that the performance of the tuning procedure is closely tied to the performance of the controllers, which are indeed fulfilling their objectives related to providing ancillary services to the grid. It is also important that the controllers are fast and react quickly to changes, especially during frequency events where time is of the essence to prevent cascade failures. In this perspective, the tuning performs excellent as the rising times of both the active and reactive powers during changes are very fast, and the DC voltage is kept well within its allowed deviation area. Discussions revolving the simplifications used during the tuning procedure are provided, and based on this it can be concluded that, for the sake of this research, the established tuning procedure is satisfactory. However, imperfections have been pointed out, and thus more work can be done to further perfect the tuning procedure.

References

[1] European-Commission. A policy framework for climate and energy in the period from 2020 to 2030. Technical report, European Union, 2014.

[2] Brian Parkin. Subsidy-free green power may be closer than you think in germany, 2019. Available at https://www.bloomberg.com/news/articles/2019-06-17/subsidy-free-green-power-may-be-closer-than-you-think-in-germany, Collected 2019-08-27.

[3] Ivan Komusanac, Daniel Fraile, and Guy Brindley. Wind energy in europe in 2018 - trends and statistics. Technical report, Wind Europe, 2019.

[4] James F. Manwell, Jon G. McGowan, and Anthony L. Rogers. *Wind Energy Explained: Theory, Design and Application*. John Wiley and Sons, Ltd, 2 edition, 2010.

[5] Olimpo Anaya-Lara. Lecture notes elk12 - wind power in electric power systems - ntnu, 2019. Unpublished.

[6] Qing-Chang Zhong, Zhenyu Ma, Wen-Long Ming, and George C. Konstantopoulos. Grid-friendly wind power systems based on the synchronverter technology. *Energy Conversion and Management*, 89:719 – 726, 2015.

[7] Q. Zhong and G. Weiss. Static synchronous generators for distributed generation and renewable energy. In *2009 IEEE/PES Power Systems Conference and Exposition*, pages 1–6, 3 2009.

[8] Q. Zhong and G. Weiss. Synchronverters: Inverters that mimic synchronous generators. *IEEE Transactions on Industrial Electronics*, 58(4):1259–1267, 4 2011.

[9] Zhenyu Ma and Qing-Chang Zhong. Synchronverter-based control strategy for back-to-back converters in wind power applications. *IFAC Proceedings Volumes*, 45(21):349 – 354, 2012. 8th Power Plant and Power System Control Symposium.

[10] A. P.B and K. N. Chandra Bose. Synchronverter based hvdc transmission for stability improvement. In *2019 International Conference on Intelligent Computing and Control Systems (ICCS)*, pages 1312–1316, 5 2019.

[11] H. Wu, X. Ruan, D. Yang, X. Chen, W. Zhao, Z. Lv, and Q. Zhong. Small-signal modeling and parameters design for virtual synchronous generators. *IEEE Transactions on Industrial Electronics*, 63(7):4292–4303, 7 2016.

[12] S. Dong and Y. C. Chen. A fast self-synchronizing synchronverter design with easily tuneable parameters. In *2018 IEEE Power Energy Society General Meeting (PESGM)*, pages 1–5, 8 2018.

[13] R. Rosso, J. Cassoli, S. Engelken, G. Buticchi, and M. Liserre. Analysis and design of lcl filter based synchronverter. In *2017 IEEE Energy Conversion Congress and Exposition (ECCE)*, pages 5587–5594, 10 2017.

[14] S. Dong and Y. C. Chen. Adjusting synchronverter dynamic response speed via damping correction loop. *IEEE Transactions on Energy Conversion*, 32(2):608–619, 6 2017.

[15] S. Dong, J. Jiang, and Y. C. Chen. Analysis of synchronverter self-synchronization dynamics to facilitate parameter tuning. *IEEE Transactions on Energy Conversion*, 35(1):11–23, 3 2020.

[16] A. R. Brahma, S. Kumaravel, V. Thomas, and S. Ashok. Impact of system parameters on the performance of synchronverter. In *2019 IEEE Region 10 Symposium (TENSYMP)*, pages 120–125, 6 2019.

[17] S. Dong and Y. C. Chen. A method to directly compute synchronverter parameters for desired dynamic response. *IEEE Transactions on Energy Conversion*, 33(2):814–825, 6 2018.

[18] H. Li, X. Zhang, T. Shao, T. Zheng, X. You, H. Yi, and Z. Li. Single-phase synchronverter dynamic optimization and parameters design. In *IECON 2017 - 43rd Annual Conference of the IEEE Industrial Electronics Society*, pages 7866–7871, 10 2017.

[19] K. R. Vasudevan, V. K. Ramachandaramurthy, T. S. Babu, and A. Pouryekta. Synchronverter: A comprehensive review of modifications, stability assessment, applications and future perspectives. *IEEE Access*, 8:131565–131589, 2020.

[20] Majid Mehrasa, Edris Pouresmaeil, Amir Sepehr, Bahram Pournazarian, Mousa Marzband, and João P.S. Catalão. Control technique for the operation of grid-tied converters with high penetration of renewable energy resources. *Electric Power Systems Research*, 166:18 – 28, 2019.

[21] Majid Mehrasa, Edris Pouresmaeil, Amir Sepehr, Bahram Pournazarian, and João P.S. Catalão. Control of power electronics-based synchronous generator for the integration of renewable energies into the power grid. *International Journal of Electrical Power Energy Systems*, 111:300 – 314, 2019.

[22] Zhou Wei, Chen Jie, and Gong Chunying. Small signal modeling and analysis of synchronverters. In *2015 IEEE 2nd International Future Energy Electronics Conference (IFEEC)*, pages 1–5, 11 2015.

[23] Q. Zhong, P. Nguyen, Z. Ma, and W. Sheng. Self-synchronized synchronverters: Inverters without a dedicated synchronization unit. *IEEE Transactions on Power Electronics*, 29(2):617–630, 2 2014.

[24] Q. Zhong, Z. Ma, and Phi-Long Nguyen. Pwm-controlled rectifiers without the need of an extra synchronisation unit. In *IECON 2012 - 38th Annual Conference on IEEE Industrial Electronics Society*, pages 691–695, 10 2012.

Table 2: System Parameters of the Test System.

Parameter	**Value**
Turbine radius, R	$12.5\,m$
Rated wind speed, $v_{w,rated}$	$12\ m/s$
Maximum power coefficient, $C_{p,max}$	0.411
Optimal tip speed ratio, λ_{opt}	7.95
Air density, ρ	$1.2\,kg/m^3$
Rated power, S_{rated}	$200\,kVA$
Switching frequency, f_s	$5\,kHz$
Nominal grid frequency, f_n	$50\,Hz$
Nominal Line-Line voltage, $V_{gn,L-L}$	$690\,V$
Nominal DC link voltage, $V_{DC,ref}$	$1126.8\,V$
Nominal DC link current, $I_{n,DC}$	$177.5\,A$
Number of pole pairs PMSG, p	28
Permanent magnet flux, Ψ	$1.7933\,Vs$
Inertia of the PMSG, J	$10\,kgm^2$
Friction factor of the PMSG, D	$0\,Nms$
DC link capacitance, C_{DC}	$10\,mF$
Chopper resistance, $R_{chopper}$	$6.3891\,\Omega$
"Stator" inductance, L_s	$0.75774\,mH$
"Stator" resistance, R_s	$0.0024\,\Omega$
Grid inductance, L_g	$0.75774\,mH$
Grid resistance, R_g	$0.0024\,\Omega$
Filter capacitance, C	$98.95\,\mu F$
Parallel resistance, R_C	$1000\,\Omega$
Virtual inductance, L_{sync}	$3\,mH$
Virtual resistance, R_{sync}	$24\,\mu\Omega$

[25] J. J. Grainger and W. D. Stevenson. *Power System Analysis*. New York: McGraw-Hill, 1994.

[26] Z. Ma, Q. Zhong, and J. D. Yan. Synchronverter-based control strategies for three-phase pwm rectifiers. In *2012 7th IEEE Conference on Industrial Electronics and Applications (ICIEA)*, pages 225–230, 7 2012.

[27] Siegfried Heier. *Grid integration of wind energy : onshore and offshore conversion systems*. Wiley, Chichester, England, 3rd ed. edition, 2014.

[28] J. G. Slootweg, H. Polinder, and W. L. Kling. Representing wind turbine electrical generating systems in fundamental frequency simulations. *IEEE Transactions on Energy Conversion*, 18(4):516–524, 12 2003.

A Appendix

A.1 System Parameters

A.2 Maximum Power point Tracking

A part of the objective for the grid side inverter is to follow the maximum power point tracking (MPPT) of the wind turbine. The power available from the turbine can be found using the simplified turbine model by Heier [27]. Here, the kinetic energy in the airflow that can be converted into mechanical power, P_m, is given by (37) where ρ is the density of the air, R is the turbine radius, v_w is the wind speed and C_p is the power

coefficient.

$$P_m = \frac{1}{2}\rho\pi R^2 v_w^3 C_p(\lambda, \beta) \tag{37}$$

The power coefficient, C_p, is dependent on the pitch angle of the turbine blades, β, and the tip speed ratio λ. λ is defined in (38), where ω_m is the rotational speed of the rotor.

$$\lambda = \frac{\omega_m R}{v_w} \tag{38}$$

All wind turbine designs have their own specific expression describing C_p. However, according to Slootweg et al [28], these expressions does not have large differences and can therefore be approximated by an analytic function. Therefore the model in (39) is used [27].

$$C_p(\lambda, \beta) = 0.5(\frac{116}{\lambda_i} - 0.4\beta - 5)e^{\frac{-21}{\lambda_i}} \tag{39}$$

Here λ_i is defined as in (40).

$$\frac{1}{\lambda_i} = \frac{1}{\lambda + 0.08\beta} - \frac{0.035}{\beta^3 + 1} \tag{40}$$

Based on the model outlined above, the turbine needs to maintain its optimal tip speed ratio, λ_{opt}, at any given wind speed to extract maximum power out of the airflow. The maximum power of the turbine, $P_{m,opt}$, can then be calculated directly in (41) based on the wind speed and the maximum power coefficient, $C_{p,max}(\lambda_{opt}, \beta)$.

$$P_{m,opt} = \frac{1}{2}\rho\pi R^2 v_w^3 C_{p,max} \tag{41}$$

To account for losses, the power set point of the inverter is set slightly lower than the MPPT value as

$$P_{ref,MPPT} = 0.95 P_{m,opt}. \tag{42}$$